GEOPHYSICS, VOL. 84, NO. 2 (MARCH-APRIL 2019); P. ID1–ID12, 13 FIGS., 4 TABLES.
10.1190/GEO2018-0168.1

Statistical modeling for real-time pore pressure prediction from predrill analysis and well logs

Jacopo Paglia[1], Jo Eidsvik[1], Arnt Grøver[2], and Ane Elisabet Lothe[2]

ABSTRACT

The challenge of pore pressure prediction in an overpressured area near a well is studied. Predrill understanding of pore pressure is available from a 3D geologic model for pressure buildup and release using a basin modeling approach. The pore pressure distribution is updated when well logs are gathered while drilling. Sequential Bayesian methods are used to conduct real-time pore pressure prediction, meaning that every time new well logs are available, the pore pressure distribution is automatically updated ahead of the bit and in every spatial direction (north, east, and depth), with associated uncertainty quantification. Spatial modeling of pore pressure variables means that the data at one well depth location will also be informative of the pore pressure variables at other depths and lateral locations. A workflow is exemplified using real data. The prior model is based on a Gaussian process fitted from geologic modeling of this field, whereas the likelihood model of well-log data is assessed from data in an exploration well in the same area. Results are presented by replaying a drilling situation in this context.

INTRODUCTION

Prediction of abnormal pore pressure is an important part of subsurface modeling. It is controlled by pressure generating and dissipating geologic processes that have taken place over millions of years. It is also determined by the fault pattern and how a sedimentary basin with pressure compartments has been formed over years. This process is essential for understanding current-day pore pressure distributions, which are important in exploration and development drilling operations. Accurate pore pressure prediction helps avoid drilling risks because it allows improved tuning of the mud weights and one can reduce drilling costs by wisely choosing the casing point before entering the reservoir or some high-pressure formation, see, e.g., Rommetveit et al. (2010) or Gholami et al. (2015).

The focus of this paper is pore pressure prediction from predrill assessments and well-log measurements. We present a new approach for real-time prediction of pore pressure, using the predrill assessment as a prior distribution, and updating the distribution when new measurements become available while drilling. First, a basin modeling approach, building on interpreted seismic horizons, and 3D pressure modeling is used for predrill evaluation. Then, the pore pressure distribution ahead of the bit and at other lateral and depth locations is updated by integrating well-log information while drilling. This modeling approach is connected to a system or workflow for automized updating of pore pressure, which is important for improved decision making. Note that seismic velocities could also be used for predrill assessment of pore pressure (Dutta, 2002; Sayers et al., 2002; Chopra and Huffman, 2006; Ugwu, 2015). In some depositional systems, such data would give a more refined predrill model, of course at the cost of extracting more information from the data.

There exist several rock-physics models that relate pore pressure to petrophysical or geophysical variables. Eaton's method (Eaton, 1975) is extensively used for pore pressure estimation from resistivity or sonic traveltime data. Bowers (1995) also proposes a method for pore pressure estimation based on velocity data. Zhang (2011) includes a depth-dependent normal compaction trend line in Eaton's methods, developing a new method for pore pressure prediction from porosity. In the current paper, we build on Zhang's equation, and we use data to learn free model parameters within that functional relationship.

Because the predictions of pore pressure are commonly applied to make decisions about the well mud weight and casing points, it is critical to get some realistic level of the uncertainty in the prediction (López et al., 2004; Wessling et al., 2013). We advocate Bayesian modeling, which naturally allows for consistent uncertainty quantification as part of the workflow. Bayesian statistics have been applied to pore pressure prediction previously: Malinverno et al. (2004)

Manuscript received by the Editor 6 March 2018; revised manuscript received 20 September 2018; published ahead of production 03 December 2018; published online 11 February 2019.
[1]NTNU, Department of Mathematical Sciences, Trondheim, Norway. E-mail: jacopo.paglia@ntnu.no; jo.eidsvik@ntnu.no.
[2]SINTEF Industry, Exploration and Reservoir Technology Group, Trondheim, Norway. E-mail: arnt.grover@sintef.no; aneelisabet.lothe@sintef.no.

use a Bayesian method to update pore pressure predictions based on logs and check shot information, with relations provided by Eaton's equations. Bektas et al. (2015) apply a sequential modeling approach to pore pressure prediction. Oughton et al. (2017) use a Bayesian network model to connect the pore pressure variables at different depths, and to different kinds of data. These approaches are similar to what we are doing here, but without the same focus on the spatial modeling aspect and on learning the prior and likelihood models from data. In the current paper, we also conduct a sensitivity analysis to different input parameters in this model and we evaluate the effect of different data on the pore pressure distribution.

The paper is organized as follows. We start with a background description of the main parts required to conduct real-time pore pressure prediction. Then, we outline the prior model, the likelihood fitting, and the sequential updating method for real-time prediction. Results and discussion are based on a real-data case.

PROBLEM DESCRIPTION

The pore pressure is denoted as $\mathbf{p} = (p_1, \ldots, p_n)$, where $p_i = p(\mathbf{s}_i)$ is the pore pressure at spatial location $\mathbf{s}_i = (s_{i1}, s_{i2}, s_{i3})$, represented by the north, east, and depth coordinates, and n is the number of locations. The predrill information about the pore pressure consists of geologic understanding of the sediments based on the interpreted reflection seismic horizons and interpreted faults. The simulated pore pressure in the predrill case is a result of modeling pressure generation and dissipation in 3D over millions of years.

The well-log data are denoted as $\mathbf{y}_j$, where the index j refers to data collected over the well path order $j = 1, \ldots, N$ and N is the total number of data points considered. We can further clarify this by using notation $\mathbf{y}_j(\mathbf{s}_{w,j})$, indicating that the well is at spatial location $\mathbf{s}_{w,j}$ at step j. In our case, we consider resistivity logs (r), neutron porosity (ϕ) and acoustic logs of traveltime (Δt), so that data are $\mathbf{y}_j = (r_j, \phi_j, \Delta t_j)$. Figure 1 illustrates the situation in which the pore pressure variables are represented on a regular 3D grid, and the well trajectory is oriented vertically.

When the drilling operation starts, the goal is to assimilate data in real time. This means that the data $\mathbf{y}_1, \ldots, \mathbf{y}_N$ are assimilated in a sequential manner, and one obtains step-wise updating of the distribution for the pore pressure variables $\mathbf{p}$ at all grid locations.

Our suggested workflow for pore pressure prediction is as follows:

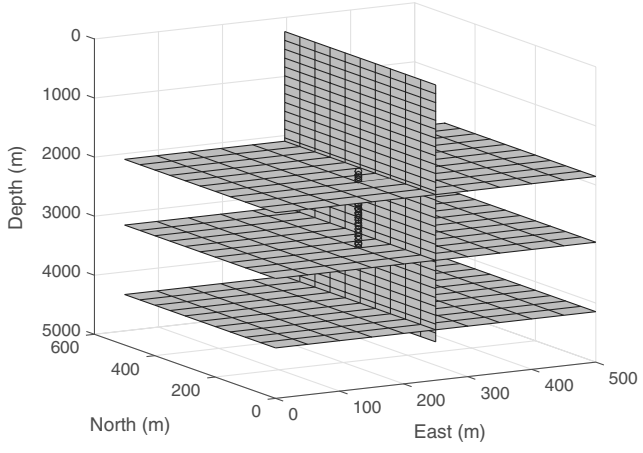

Figure 1. Illustration of slices of a 3D grid covering a subsurface domain. At each site in the grid, we aim to predict the pore pressure. The black points represent the well path where resistivity, neutron porosity, and traveltime log data are gathered.

1) Train a prior distribution from pore pressure variables obtained from geologic modeling.
2) Specify the likelihood model for well-log data based on the available logs in the vicinity of the current location.
3) Use a sequential updating method for real-time pore pressure prediction.

We will go through these steps in the next three sections.

PRIOR MODEL — PREDRILL ASSESSMENT FROM GEOLOGIC MODELING

We construct a multivariate prior distribution for pore pressure variables in the subsurface domain by using extensive predrill assessment based on geologic modeling. In our case, the predrill information is given by Pressim (Borge, 2000; Lothe, 2004), which is software developed by SINTEF Petroleum Research. Pressim is a tool for modeling pressure generation and dissipation within sedimentary basins over geologic time. The modeled pressure generation is controlled by the degree of mechanical and chemical compaction, whereas the pressure dissipation and lateral pressure transfer is controlled by flow barriers such as faults and low permeable sedimentary units such as shales or salt. The pressure generation due to compaction and diagenesis, and dissipation due to hydraulic failure and leakage (Lothe et al., 2004), is calculated from burial and possible uplift in the study area (Lothe and Grøver, 2009). Overall, the modeled present-day pressure distribution within the basin is a result of its burial history.

A sedimentary basin is a dynamic system over geologic time. It may experience periods with rapid burial leading to a high degree of compaction, but also periods with sediment erosion and uplift leading to high degree of pressure dissipation due to fracturing and leakage. The sediment rock physical properties such as permeability, and the sealing properties of the fault zones may accordingly change with time. The change in porosity is in Pressim given by compaction curves (Sclater and Christie, 1980) and kinetic equations reflecting the degree of chemical compaction, such as quartz growth in sandstone reservoir controlled by the temperature (Walderhaug, 1996). The tool quantifies pressure dissipation using a model for lateral cross-fault fluid flow, and Darcy's flow equation in the vertical direction. The sediment permeability is given by Kozeny-Carman equations (Mavko et al., 2009), linked to its lithology and associated calculated porosity. The modified Griffith-Coulomb failure (Jaeger and Cook, 1963) and the frictional-sliding criterion (Twiss and Moores, 1992) are included to simulate hydraulic leakage from overpressured compartments. We get the sand clay fraction from existing well logs, to set up the geomodel. The quality of the modeled pressure distribution is given by the misfit with observed pressure values at existing well locations.

A general pitfall with this basin modeling approach is the large number of input parameters, their inherent uncertainty, as well as the uncertainty of the process model itself. Several inputs may give similar fit to observations. To capture these issues of the complex problem, a Monte Carlo approach is used, in which the input parameters to the geologic model are varied (Lothe and Grøver, 2009). In our setting, we only consider a few Monte Carlo realizations and we only study the pore pressure at the present time.

Figure 2 shows the spatial structure of the field under consideration. Based on the interpreted reflection seismic and interpreted faults, the study area is divided into 18 depth layers of various thick-

ness (Figure 2a) and 41 vertical compartments (Figure 2b). The overburden shales are rather flat in the study area, whereas the reservoir forms a dome structure. The faults have minor throw; see the model description in Lothe et al. (2018). Figure 2b shows color-coded compartments and many other minor faults. Predrill pressure simulations are carried out for the last 34 millions years, using forward modeling with the pressure calculated every 10,000 years.

Figure 3 shows simulated pore pressure as a function of depth for all the compartment locations in the study area, together with the hydrostatic pressure and the overburden stress, which are also given from the predrill model. We notice a trend of increasing pore pressure as a function of depth. The predrill model predicts that pore pressure is close to the hydrostatic pressure (normal pressure, the red line in Figure 3) for the first 1000 m, then we have overpressure (abnormal pressure). The overpressures from 1000 to 3000 m in the shaly overburden are mainly generated by the illite-smectite diagenesis (Lothe et al., 2018). At depths between 3000 and 4000 m, the model predicts a drop in pore pressure that remains well above the hydrostatic pressure. Less than 4000 m there seems to be increased pore pressure, which is closer to the overburden stress (the blue line in Figure 3). The ability of the predrill model to predict pressures correctly has been tested in several different study areas, such as the Halten terrace area (Lothe, 2004) and northern North Sea (Borge, 2000), with positive results.

One reason for conducting real-time pore pressure updating is to make improved decisions related to drilling mud weight in regions where there is overpressure. For the case that we are considering, the mud weight specification is associated with pore pressure relative to the hydrostatic and overburden pressure. It is for this reason natural to build a statistical model in which we avoid values of pore pressure lower than hydrostatic pressure or greater than the overburden stress. Hence, we introduce the following constraints:

$$p_{h_i} < p_i < p_{ob_i} \quad i = 1, \ldots, n, \tag{1}$$

where p_{h_i} represents the fixed hydrostatic pressure and p_{ob_i} is the fixed overburden stress, at (depth of) location $\mathbf{s}_i$. Statistical modeling with constraints can be difficult, and one standard way to go around this is to use another variable $x_i \in (-\infty, \infty)$ defined by a logistic transform (Dobson and Barnett, 2008) as follows:

$$x_i = \log\left(\frac{p_i - p_{h_i}}{p_{ob_i} - p_i}\right) \quad i = 1, \ldots, n. \tag{2}$$

We will base the prior model on this transformed pore pressure variable. The pore pressure p_i at location $\boldsymbol{s}_i$ can be directly computed from x_i by the inverse of equation 2:

$$p_i = \frac{e^{x_i} p_{ob_i} + p_{h_i}}{1 + e^{x_i}} \quad i = 1, \ldots, n. \tag{3}$$

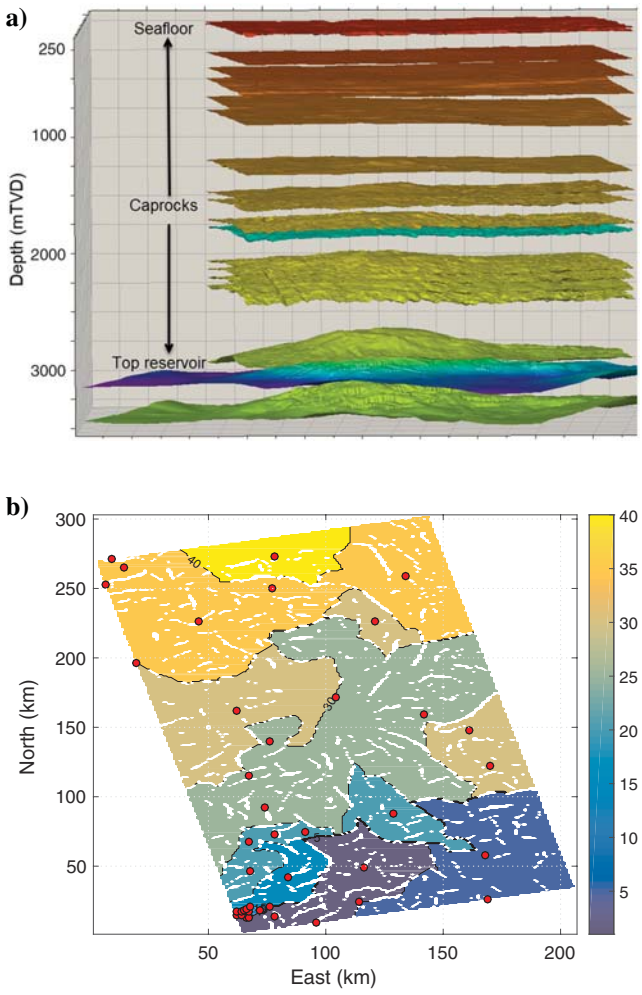

Figure 2. Geometry of the available predrill information. Based on the interpreted seismic horizons used in the Pressim geomodel, the study area is divided in 18 horizontal layers of various thickness and 41 vertical compartments. (a) Vertical view of the field. (b) Map view, the faults only partially seal the compartments. Circles indicate geometric centers of compartments and constitute the sites where prior information were available. The colorbar helps to identify the compartments.

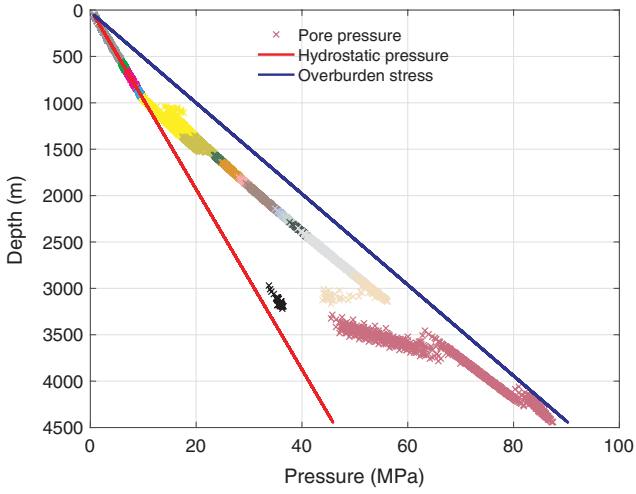

Figure 3. Predrill pore pressure (colored) plotted as a function of depth together with the hydrostatic pressure (red) and the overburden stress (blue) that are also given from the predrill model. The different colors indicate the different layers in which the information about pore pressure is obtained. The model predicts normal pressure for the first 1000 m and then the overpressure starts, and even though there is a drop in the predicted pore pressure between 3000 and 4000 m, the pore pressure remains well above the hydrostatic pressure.

We now build a prior model for the transformed pore pressure at all locations, i.e., $\mathbf{x} = (x_1, \ldots, x_n)$. We construct a multivariate Gaussian distribution in which regression models represent the prior mean as a function of layers and depth, and where variograms are used to study the spatial variability and correlation between the sites of the grid. For each layer k of the overpressured area, focusing then on the deeper layers ($k \geq 6$):

$$x_{i_k,k} = \beta_{0,k} + \beta_{1,k} s_{i_k 3,k} + \epsilon_{i_k,k} \quad k = 6, \ldots, 18, \tag{4}$$

where $(s_{i_k 3,k}, x_{i_k,k})$ represent the depth and logistic pore pressure defined in equation 2, observed in layer k, and at coordinate $i_k \in I_k = \{1, \ldots, n_k | n_k \text{ number of sites in layer } k\}$. We assume that $\mathbb{E}(\epsilon_{i_k,k}) = 0$ and that the variance is constant, $\mathrm{Var}(\epsilon_{i_k,k}) = \sigma_k^2$ for each $i_k \in I_k$. The estimates of the regression intercept $\beta_{0,k}$ and slope $\beta_{1,k}$ are derived using the method of least squares. We then specify the regression coefficients $\hat{\beta}_{1,k} = \sum_{i_k \in I_k}(x_{i_k,k} - \bar{x}_k)(s_{i_k 3,k} - \bar{s}_{3,k}) / \sum_{i_k \in I_k}(s_{i_k 3,k} - \bar{s}_{3,k})^2$ and $\hat{\beta}_{0,k} = \bar{x}_k - \hat{\beta}_{1,k}\bar{s}_{3,k}$, with $\bar{x}_k$ and $\bar{s}_{3,k}$ sample means within the layer k.

Figure 4 shows the residuals of the regression analysis for layer 8 (there is similar behavior in other layers). Such residual plots are used to check if the model assumptions are fulfilled. In the histogram of the residuals, the frequency of the residual values is plotted. We notice the typical bell shape of the Gaussian distribution, equally distributed at approximately zero, confirming the modeling approach. The other plots are used to check the assumptions of constant variance of the residuals (Figure 4c) and remaining model correlation (Figure 4d).

The spatial covariance is studied further using variograms (Goovaerts, 1997) of the residuals, within the layers and between the layers. Figure 5a and 5b shows the empirical semivariograms together with fitted models.

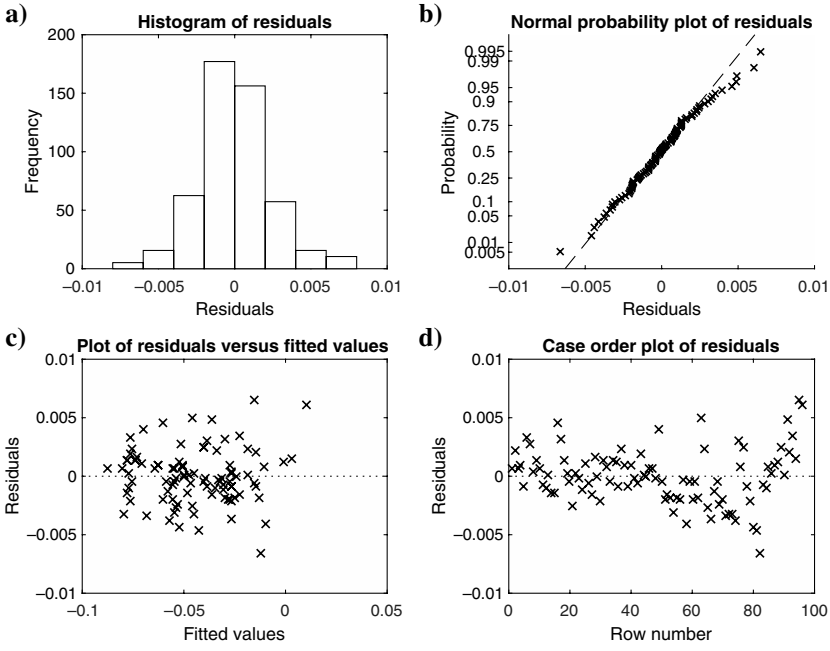

Figure 4. Residuals of the regression analysis for layer 8. (a) The histogram shows the typical symmetric bell shape of the Gaussian distribution, and (b) the normal probability plot further confirms this idea. (c) Residuals versus fitted values check the assumption of constant variance of the residuals, and because they are evenly spread at approximately zero, we can say this is fulfilled. (d) The pattern in the order plot indicates the possible residual correlation in the model.

The fitted variograms are based on the exponential model, in which the lateral and vertical functions are

$$\gamma_k(h) = \sigma_k^2 \left(1 - \exp\left(-\frac{h}{r_k}\right)\right) \quad k = 6, \ldots, 18, \tag{5}$$

$$\gamma_c(h) = \sigma_c^2 \left(1 - \exp\left(-\frac{h}{r_c}\right)\right) \quad c = 1, \ldots, 41, \tag{6}$$

where h is the distance between points, r is the range parameter of the variogram, which is indicative of correlation distance, σ_k^2 is the adjusted variance in layer k, and σ_c^2 is the adjusted variance along the compartment c. These σ values correspond to the sill representing the asymptotic level of the variogram for large distance h. Figure 5 shows how the sill value changes if we consider the semivariogram for layer or the one for column; this means that we have a larger variability within the column compared with the layers. Note that the sill value for the semivariogram in layer 8 (Figure 5a) corresponds to the variance of the residual of that layer (Figure 4).

Overall, we build the covariance matrix for the logistic pore pressure variable for any two sites by

$$\Sigma(\mathbf{s}_{i,k}, \mathbf{s}_{j,l}) = \sigma^2 \exp\left(-\frac{\sqrt{(s_{i1,k} - s_{j1,l})^2 + (s_{i2,k} - s_{j2,l})^2}}{r_1} - \frac{|s_{i3,k} - s_{j3,l}|}{r_2}\right), \tag{7}$$

where $\sigma^2 = 1/13 \sum_{k=6}^{18} \sigma_k^2$ is the average of the standard deviations (SDs) for the layers and r_1 and r_2 are the average range for the variograms per layers and per compartments.

In summary, we then have a prior distribution

$$\pi(\mathbf{x}) = N(\mathbf{x}; \mu, \Sigma), \tag{8}$$

where $N()$ denotes the multivariate Gaussian density function. The mean $\mu = (\mu_{x_1}, \ldots, \mu_{x_n})$ depends on the fitted regression parameters derived by least squares for equation 4, and the covariance matrix Σ is defined in equation 7.

Recall that the pore pressure p_i is defined from equation 3. Even though we always work with the transformed variable x_i, we plot and interpret results for the pore pressure p_i. The distribution of pore pressure can be approximated using, for instance, a first-order Taylor expansion of equation 3 centered in μ_{x_i}. We then get

$$p_i(x_i) \approx p_i(\mu_{x_i}) + p_i'(\mu_{x_i})(x_i - \mu_{x_i}) \quad i = 1, \ldots, n, \tag{9}$$

and so

$$\mathbb{E}(p_i) \approx p_i(\mu_{x_i}) \quad i = 1, \ldots, n, \tag{10}$$

$$\mathrm{Var}(p_i) \approx (p_i'(\mu_{x_i}))^2 \mathrm{Var}(x_i) \quad i = 1, \ldots, n. \tag{11}$$

A similar approach can be used for the multivariate properties of the pore pressure.

In Figure 6, we show the resulting mean and 90% prior prediction interval for the pore pressure, as well as the correlation matrix. This is representative of the 3D grid shown in Figure 1.

The correlation is here organized according to the layers, and we notice great dependence within layers and between sites that are close. When the distance between locations increases, the correlation gets very low.

LIKELIHOOD MODEL — SPECIFICATION FROM WELL-LOG DATA AND PHYSICAL MODELS

The likelihood model should describe the probability distribution of well-log responses as a function of pore pressure. There are several rock-physics relations linking pore pressure to petrophysical and geophysical variables (Mavko et al., 2009). However, they are often complicated by multivariable interactions in the relations, and they tend to work in specific environments, for instance, depending on the compaction as in the Gulf of Mexico (Sayers et al., 2005). It is known that porosity depends on pore pressure, but it also depends on the lithologic composition and other attributes. Therefore, it is difficult to extract pore pressure from porosity unless we know the other variables going into the equation, or know that the study is representative of an area where rapid subsidence and compaction is the main driving mechanism. The same is true for other petrophysical variables. Thus, the specification of a likelihood model would be case specific. We build our likelihood model using the existing relation by Zhang (2011), and we train free model parameters from well-log data. Other models could be equally applicable, but a similar workflow would hold. In the following, we outline the assumptions going into our procedure.

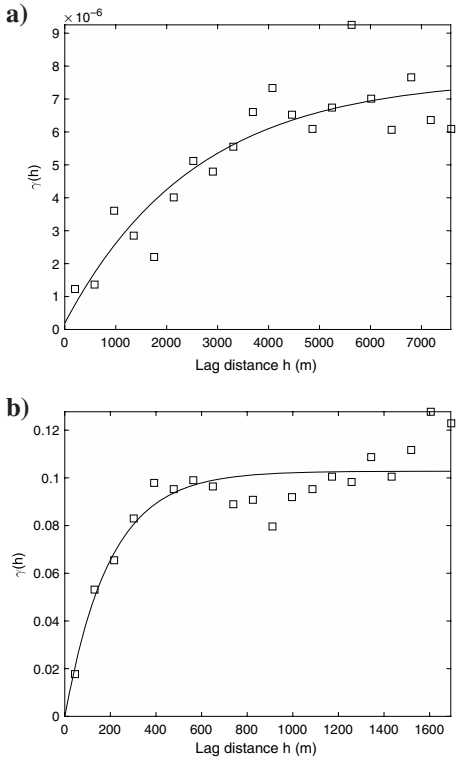

Figure 5. Empirical and fitted exponential semivariograms as function of the lag distance. (a) Layer 8, (b) compartment 41.

The likelihood model is specified from measurements acquired in a well in the same field (the data are provided by ConocoPhillips and the Norwegian Petroleum Directorate). The data consist of logs within a depth domain of the formation. We focus our attention on resistivity, neutron porosity, and sonic logs, as well as gamma ray data.

Figure 7 shows the data as a function of measured depth (MD). We choose to focus on this specific depth interval (3105–3420 m) because it corresponds to an area where all the data are available. We notice that we have much larger resistivity values near 3200 m. This is an oil-saturated zone. Likewise, we have a much larger gamma ray at approximately 3240 m, representing the interval in which we pass from the upper formation to the lower formation.

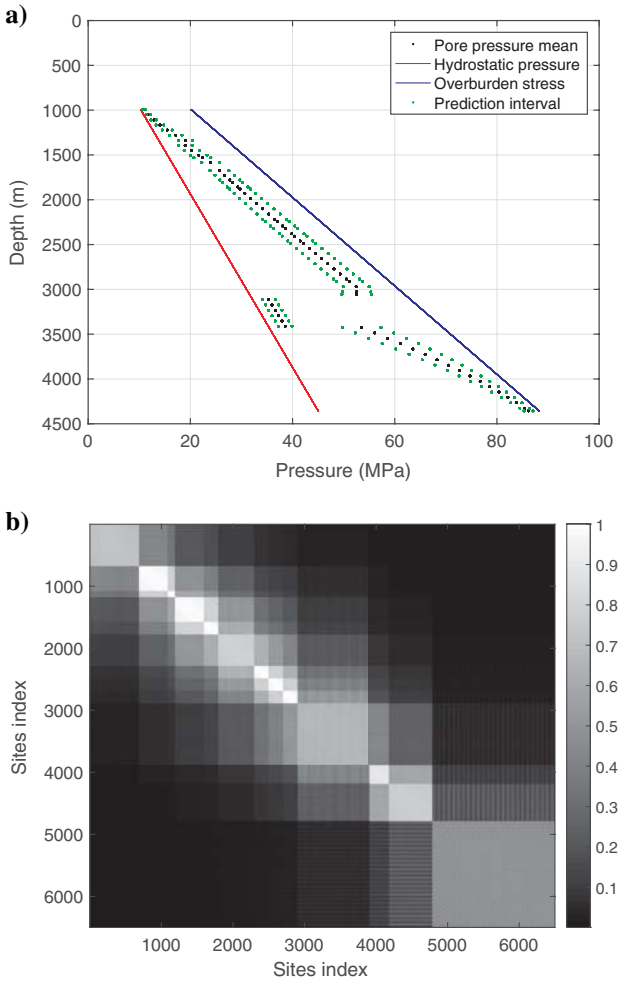

Figure 6. The prior model for pore pressure is a multivariate Gaussian distribution with mean μ and covariance Σ. The dimension is given by the number of sites in the spatial grid. (a) Pore pressure prior mean (black) with a 90% prediction interval (green) together with the hydrostatic pressure and the overburden stress. (b) Prior correlation matrix for pore pressure. It is organized according to the layers, meaning that each site of the grid is sequentially assigned to an index. For close sites the difference of the respective site indexes will be low. The correlation matrix helps to highlight the large correlation within layers and between sites that are close.

We decided to remove these parts (the dashed depth zone in Figure 7) from the data set because they would distract the focus on modeling the pore pressure. This is commonly done in inverse problems because there are many possibilities for getting the same response, and some parameters must be fixed in the modeling, whereas others are treated as random and assigned distributions (Malinverno and Parker, 2006). In the current setting, there are also other inputs, such as temperature and salinity, which influence the response, but they are quite well-known for the North Sea (Bhakta et al., 2016), and not considered in this study.

The likelihood model tying pore pressure to log measurements is here represented by a Gaussian distribution with nonlinear expected values based on rock-physics relations described by Zhang (2011). Given a pore pressure input, the model for resistivity, porosity, and transit time measurements is defined by

$$\mathbf{y}_j = \begin{pmatrix} r_j \\ \phi_j \\ \Delta t_j \end{pmatrix} = \begin{pmatrix} \left(\frac{p_{ob_j}-p_j}{p_{ob_j}-p_{h_j}}\right)^{1/n_r} r_0 e^{bz_j} \\ \phi_0 \exp\left(-\frac{p_{ob_j}-p_j}{p_{ob_j}-p_{h_j}} c_\phi z_j\right) \\ (\Delta t_{ml}-\Delta t_m)\exp\left(\frac{p_j-p_{ob_j}}{p_{ob_j}-p_{h_j}} c_t z_j\right)+\Delta t_m \end{pmatrix} + \begin{pmatrix} \epsilon_{r_j} \\ \epsilon_{\phi_j} \\ \epsilon_{\Delta t_j} \end{pmatrix} \tag{12}$$

$$\Rightarrow \mathbf{y}_j = \mathbf{g}_j(p_j) + \epsilon_j, \quad \epsilon_j \sim N(\mathbf{0}, \mathbf{R}), \quad j = 1, \ldots, N. \tag{13}$$

The 3×1 function $\mathbf{g}(p) = (\mathbb{E}(r|p), \mathbb{E}(\phi|p), \mathbb{E}(\Delta t|p))$ represents the expected values of resistivity, porosity, and transit time, given the pore pressure input, i.e., $\mathbb{E}(\mathbf{y}|p)$. The function $\mathbf{R}$ is the 3×3 measurement noise covariance matrix.

Many parameters in the expectation part of equation 12 must be specified. First, values for p_{ob} and p_h are derived from the Pressim realizations. Moreover, z_j is the depth at measurement location j. For the resistivity function, n_r is the Eaton exponent, r_0 is the normal compaction shale resistivity at the mudline, and b is the slope of logarithmic resistivity normal compaction trendline. For the porosity equation, ϕ_0 is the porosity at the mudline and c_ϕ a constant that can be derived from the normal compaction porosity trendline. Finally, in the sonic transit time function, Δt_{ml} is the compressional transit time in the shale matrix, whereas Δt_m is the mudline transit time and c_t is a constant (Zhang, 2011). These values are chosen based on the parametric form in equation 12 with parameters tuned to fit the well-log data (Table 1).

Figure 8 shows the well logs in gray, the expectation part of the functions in equation 12 in black (where the pore pressure comes from the Pressim realizations). When constructing the expectation part in these plots, we varied pore pressure between the normal pressure and the overburden stress at a depth of 3350 m and evaluated equation 12 for resistivity, porosity, and transit time.

The noise terms ϵ_j in equation 13 are assumed to be independent at different steps j, and this means that the measurements are considered to be only location-wise dependent. Hence, the likelihood model involves conditional independence such that

$$\pi(\mathbf{y}|\mathbf{x}) = \prod_j^N \pi(\mathbf{y}_j|\mathbf{x}) = \prod_j^N \pi(\mathbf{y}_j|x_j), \tag{14}$$

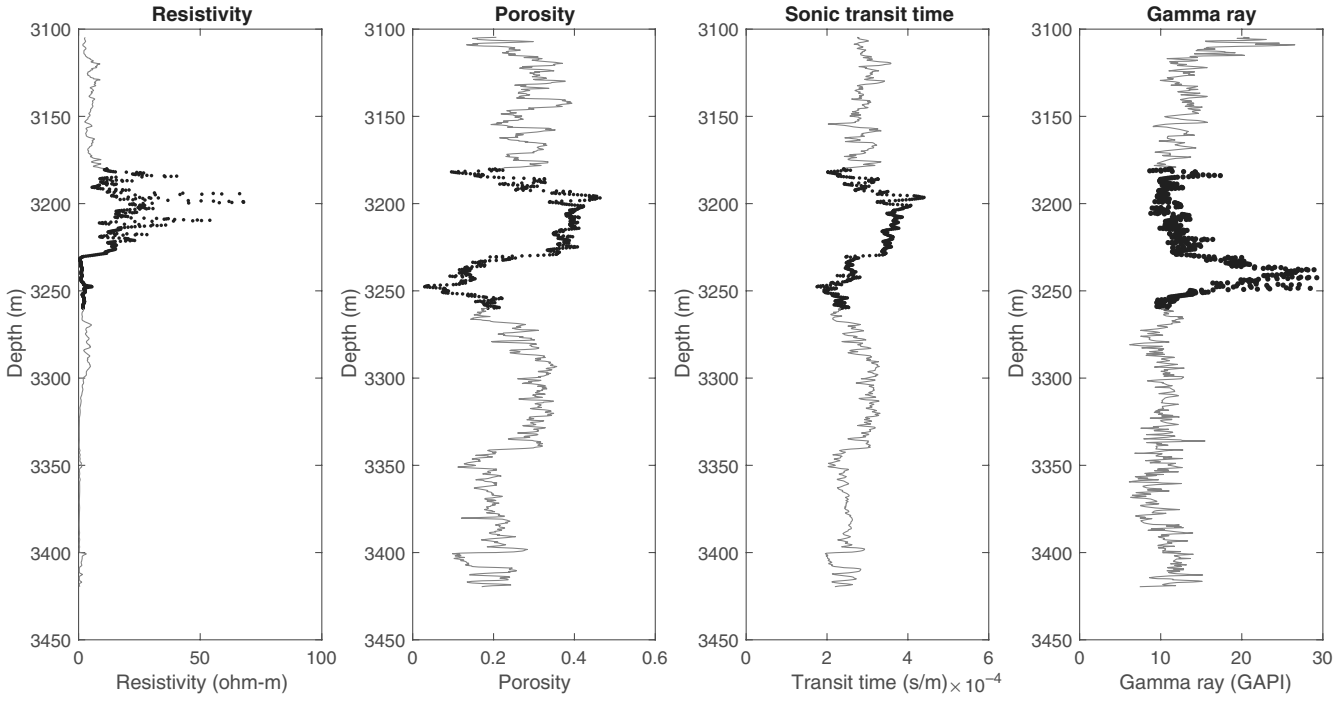

Figure 7. Well-log measurements of resistivity, neutron porosity, sonic transit time, and gamma ray as functions of the MD. In the likelihood fitting, the dashed black parts are ignored because they would distract the focus on modeling the pore pressure. The depth interval considered here goes from 3105 to 3420 m, and it corresponds to an area where all the data are available.

where, in short, $x_j = x(\mathbf{s}_{w,j})$ is the logistic pore pressure at well-log location j. From equation 13, we have

$$\pi(\mathbf{y}_j|x_j) = N(\mathbf{y}_j; \mathbf{g}_j(p_j), \mathbf{R}), p_j = p(x_j). \quad (15)$$

We assume that the error covariance matrix $\mathbf{R}$ is constant over the time steps. We next specify this covariance matrix from residual variability in the data and the rock-physics models.

Using a first-order Taylor expansion centered in μ_j, we get

$$\mathbf{g}_j(p_j) \approx \mathbf{g}_j(\mu_j) + \frac{\partial \mathbf{g}_j}{\partial p_j}|_{\mu_j}(p_j - \mu_j) \quad j = 1, \ldots, N; \quad (16)$$

Hence,

$$\mathbb{E}(\mathbf{y}_j) = \mathbf{g}_j(\mu_j) \quad j = 1, \ldots, N, \quad (17)$$

$$\mathrm{Var}(\mathbf{y}_j) = \mathbf{R} + \frac{\partial \mathbf{g}_j}{\partial p_j}\Big|_{\boldsymbol{\mu}_j} \mathrm{Var}(p_j) \frac{\partial \mathbf{g}_j}{\partial p_j}\Big|_{\boldsymbol{\mu}_j}^t \quad j = 1, \ldots, N. \quad (18)$$

From equation 18, we then obtain an estimate for the covariance $\mathbf{R}$

$$\hat{\mathbf{R}} = \frac{\sum_{j=1}^{N}(\mathbf{y}_j - \mathbf{g}_j(\mu_j))(\mathbf{y}_j - \mathbf{g}_j(\mu_i))^t}{N} - \frac{\partial \mathbf{g}_j}{\partial p_j}\Big|_{\boldsymbol{\mu}_j} \mathrm{Var}(p_j) \frac{\partial \mathbf{g}_j}{\partial p_j}\Big|_{\boldsymbol{\mu}_j}^t. \quad (19)$$

Here, the variance $\mathrm{Var}(p_j)$ is constant because all the well-log sites belong to the same layer.

Applying the previous calculation to the data, we get

$$\hat{\mathbf{R}} = \begin{pmatrix} 6.8137 & 0.1503 & 8.5835 \times 10^{-5} \\ 0.1503 & 0.0083 & 4.4036 \times 10^{-6} \\ 8.5835 \times 10^{-5} & 4.4036 \times 10^{-6} & 2.5930 \times 10^{-9} \end{pmatrix}. \quad (20)$$

We see that there is some correlation in the data, in particular between resistivity and porosity. Not only do the variances indicate measurement errors, but they are also a result of how well the equations in our model fit the data. The resistivity error is very large, compared with that of porosity and sonic transit time. This is also clear from Figure 9, in which the center lines show the likelihood functions in equation 12 plotted as a function of pore pressure

Table 1. Parameter values for equation 12.

Parameter values		
Resistivity	Porosity	Transit time
$n_r = 1.2$	$\phi_0 = 0.574$	$\Delta t_{ml} = 0.65 \times 10^{-3}$ s/m
$r_0 = 0.43$ ohm-m	$c_\phi = 0.39 \times 10^{-3}$ m^{-1}	$\Delta t_m = 0.20 \times 10^{-3}$ s/m
$b = 0.12 \times 10^{-4}$	—	$c_t = 0.9 \times 10^{-3}$ m^{-1}

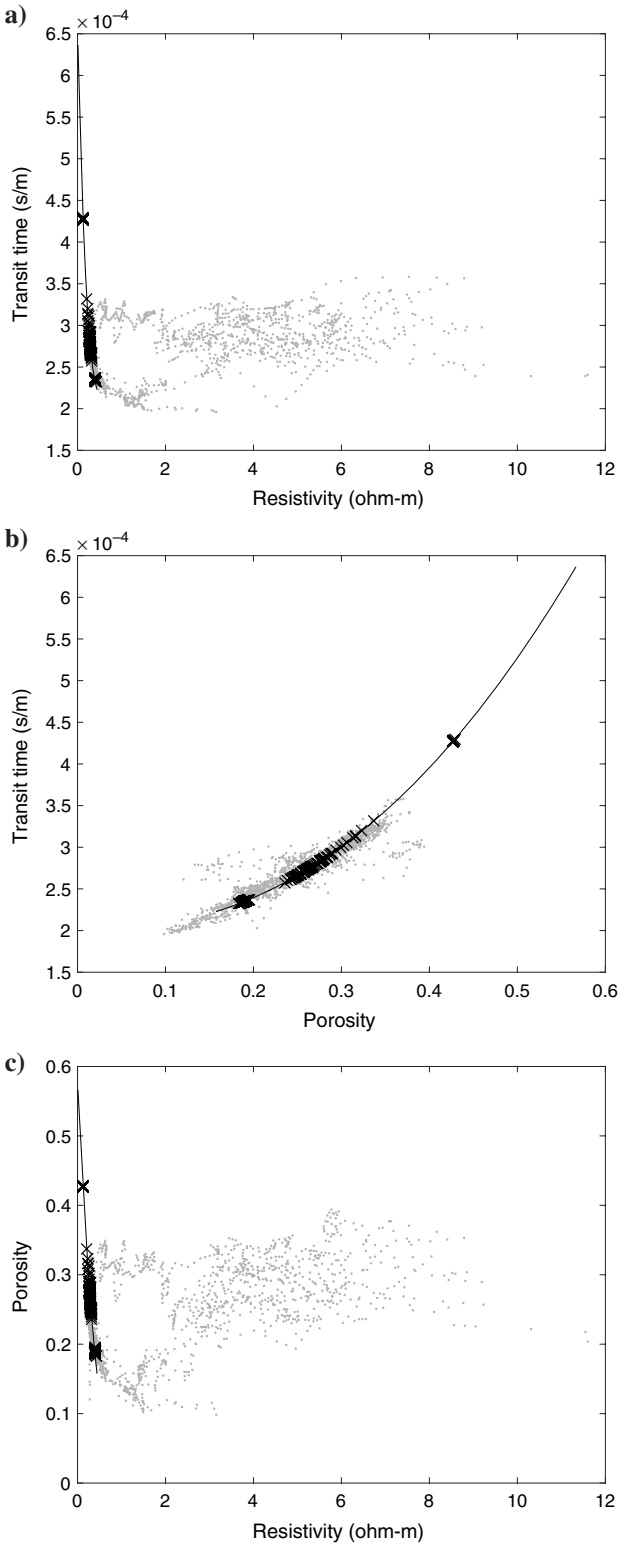

Figure 8. Crossplots of the well-log data (dots) and the expected value in the likelihood (black is the functional link, and the cross is this function evaluated at pressure outputs around the same depth with Pressim output).

varying between the hydrostatic pressure and the overburden stress at a given depth of 3350 m.

It appears as if the porosity and transit time are relatively accurate, based on our model errors, and these data should likely provide useful information about the pore pressure variables in our situation.

SEQUENTIAL UPDATING

The Bayesian formalism, with a prior model for pore pressure variables and likelihood models for the data, is suitable for consistent assimilation of multiple data sources. In our case, the goal is to perform real-time updating of the pore pressure, at any location, when data are acquired in the well. This means that we include well-log data in a step-wise manner while drilling, and the posterior after one update becomes the prior for the next step, and so on.

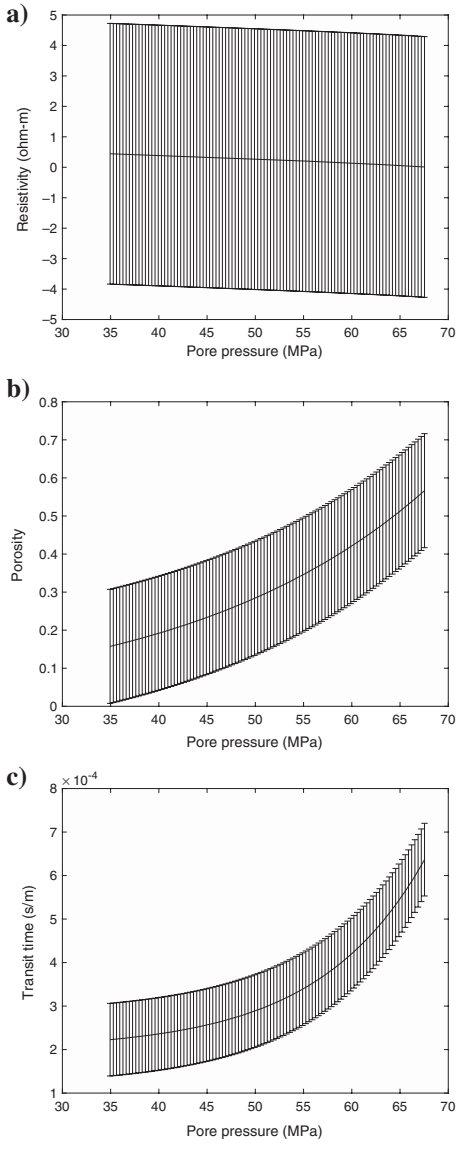

Figure 9. Likelihood equation 12 as a function of pore pressure at a fixed depth (3350 m) with vertical error bars (representing a 90% prediction interval). Here, the pore pressure varies between the hydrostatic pressure and the overburden stress at 3350 m. The figure helps in understanding the results obtained fitting the covariance matrix $\mathbf{R}$, showing the largest model error values for resistivity.

Using the transformed pore pressure variable as given in equation 2, we have the posterior distribution

$$\pi(\mathbf{x}|\mathbf{y}_1, \ldots, \mathbf{y}_j) = \frac{\pi(\mathbf{x})\pi(\mathbf{y}_1|\mathbf{x}) \ldots \pi(\mathbf{y}_j|\mathbf{x})}{\pi(\mathbf{y}_1, \ldots, \mathbf{y}_j)}$$
$$\propto \pi(\mathbf{x})\pi(\mathbf{y}_1|\mathbf{x}) \ldots \pi(\mathbf{y}_j|\mathbf{x}) \propto \pi(\mathbf{x}|\mathbf{y}_1, \ldots, \mathbf{y}_{j-1})\pi(\mathbf{y}_j|\mathbf{x}). \tag{21}$$

Here, we use the assumption that consecutive measurements along the borehole, for $j = 1, \ldots, N$, are conditionally independent, given the pore pressure variables; see equation 15. Meaning that the measurements, at a given location, depend only on the pore pressure at that location, and not on the variables at other locations. The distribution in equation 21 is assessed by a linearized approach, not dissimilar to the extended Kalman filter (Särkkä, 2013). This approach entails a linearization of the nonlinear expectation in the likelihood, with derivatives $\mathbf{G}_j = d\mathbf{g}_j/d\mathbf{x}$. The matrix $\mathbf{G}_j$ is an $m \times n$ matrix, where only the column corresponding to location $s_{w,j}$ is nonzero, whereas all other $n - 1$ columns are zero. This structure is a result of the location-wise dependence.

For the situation with a Gaussian prior and a linearized Gaussian likelihood model, the sequential updating of data leads to a Gaussian distribution $\pi(\mathbf{x}|\mathbf{y}_1, \ldots, \mathbf{y}_j)$ in equation 21. The updated mean $\mathbf{m}_j = \mathbb{E}(\mathbf{x}|\mathbf{y}_1, \ldots, \mathbf{y}_j)$ and variance $\mathbf{V}_j = \mathrm{Var}(\mathbf{x}|\mathbf{y}_1, \ldots, \mathbf{y}_j)$ are computed recursively over the data gathering steps:

- Initialization:

$$\mathbf{m}_0 = \mu, \tag{22}$$

$$\mathbf{V}_0 = \Sigma. \tag{23}$$

- Recursive updating for $j = 1, \ldots, N$:

$$\begin{aligned} \mathbf{S}_j &= \mathbf{G}_j\mathbf{V}_{j-1}\mathbf{G}_j^t + \mathbf{R}, \\ \mathbf{K}_j &= \mathbf{V}_{j-1}\mathbf{G}_j^t\mathbf{S}_j^{-1}, \\ \mathbf{m}_j &= \mathbf{m}_{j-1} + \mathbf{K}_j(\mathbf{y}_j - \mathbf{g}_j(\mathbf{m}_{j-1})), \\ \mathbf{V}_j &= \mathbf{V}_{j-1} - \mathbf{K}_j\mathbf{G}_j\mathbf{V}_{j-1}. \end{aligned} \tag{24}$$

At the last step of the algorithm, we have the posterior Gaussian distribution $\pi(\mathbf{x}|\mathbf{y}_1, \ldots, \mathbf{y}_N)$, given all the data. Recall that several model assumptions have been done. First, we assume reliable predrill information for pore pressure that takes into account all the major mechanisms for pore pressure buildup and release. Moreover, the likelihood model is assumed to represent the well observations realistically.

RESULTS

We now present the results of the sequential updating method. The idea is to study a new case, in which we replay a well centered in a 3D subsurface grid (Figure 1) and study the effect of assimilating data. The regular grid is of size 10×10 in the northeast direction ((x, y) plane), where each compartment is 50×50 m^2.

In depth (the z-direction), we keep a structure similar to the one of the prior realization, with division in layers. Data are gathered along a vertical well, and the data assimilation starts at 1674 m and terminates at 3056 m.

Data $\mathbf{y}$ are simulated using first a realization from the prior and then a realization from the likelihood in equation 12. The sequential updating method, based on this data, is applied to $\mathbf{x}$ using equation 24. Results are visualized for pore pressure $\mathbf{p}$.

Figure 10 shows the results of the sequential updating procedure at an intermediate step, whereas Figures 11 and 12 compare the prior pore pressure distribution with the posterior distribution obtained at the final step. In Figure 10, we look at a step in which data are collected up to the depth of 2913 m. Figure 10a displays the pore pressure prediction for the sites along the well path with a 90% prediction interval. Hence, the true pore pressure would be covered by prediction interval approximately 90 out of 100 times. Figure 10b visualizes the updated SD and mean for a horizontal plane at depth 3056 m, which is 143 m ahead of the bit. The conditional mean and SD of pore pressure (in MPa units) are plotted for each grid site of the plane. We note how the smallest SDs are at the sites closer to the well location, due to the spatial dependence in the prior model.

Figure 11 shows a comparison between the prior and posterior SD in pore pressure in the 3D grid. The colorbars on the side of the plot are in MPa units. Again, the spatial dependence means that the reduction in the SD is larger in the area around the well (the white points), whereas it remains similar to the prior far from the well. Figure 12 shows a comparison between the prior (the black) and posterior (the magenta) pore pressure, along the well path. In this particular case, the well-log data indicate lower pore pressure than in the prior model, and the pore pressure predictive means are reduced. The reduction in the SD gives a narrower posterior prediction interval indicating that well-log data influence the pore pressure prediction.

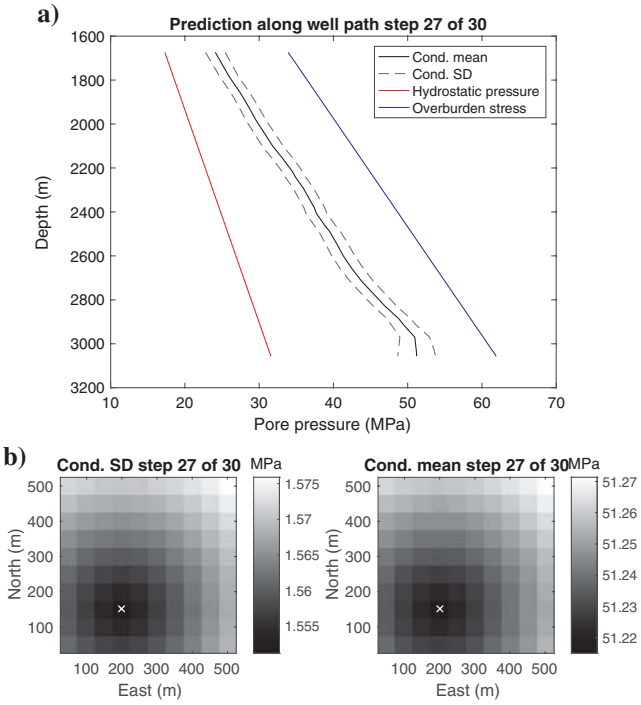

Figure 10. Intermediate step of the sequential updating; data are collected up to the depth of 2913 m. (a) Pore pressure along the well path with a 90% prediction interval. (b) SD (left) and mean (right) of pore pressure in each site of an horizontal plane at a depth of 3056 m, so 143 m ahead of the bit. The crosses indicate the well location. The lowest values of the SD are at sites closer to the well, due to the spatial dependency introduced in the prior covariance matrix.

DISCUSSION

A sensitivity analysis is carried out to study the impact of the prior and likelihood models on the results. We start by analyzing the effects of a variation of the fitted predrill assessment; we consider two variations of the prior covariance matrix. In the first situation (Case I), the covariance matrix keeps the same structure as in equation 7, but with $\sigma^2_{\text{new}} = 2 * \sigma^2$. This means that there will be greater prior uncertainty. For Case II, we include global variability in the prior. This is achieved by adding $\mathbf{z}\boldsymbol{\Sigma}_{\beta_{gl}}\mathbf{z}^T$ to the prior covariance $\boldsymbol{\Sigma}$. Here, $\mathbf{z}$ is a vector of all depth indices and $\boldsymbol{\Sigma}_{\beta_{gl}}$ represents the uncertainty (covariance matrix) for depth trends in pore pres-

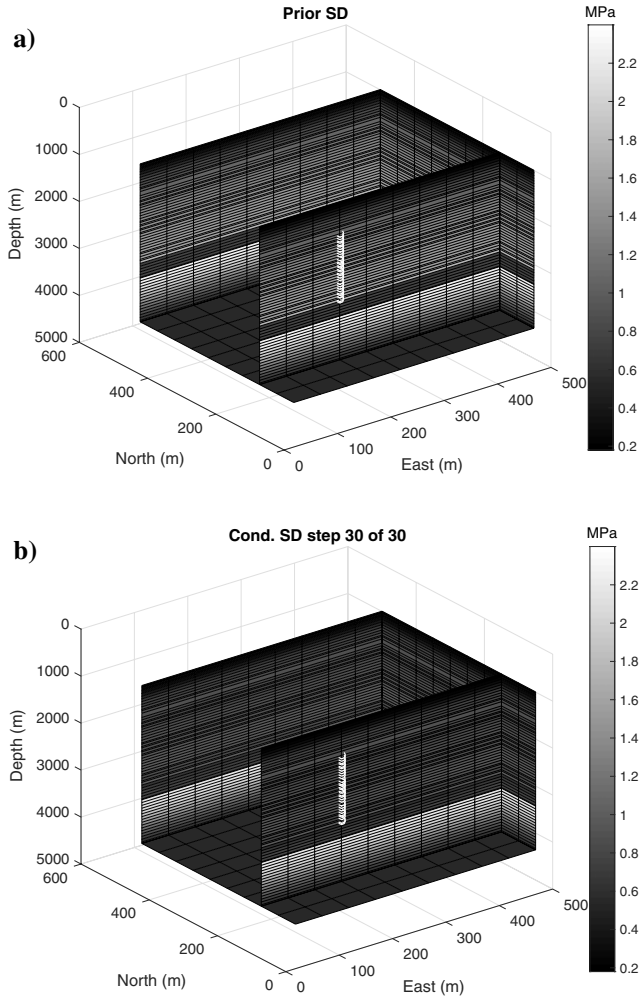

Figure 11. Comparison between (a) the prior and (b) the final pore pressure SD in a 3D grid of the area around the well (white points). There is a considerable reduction in the SD for the sites close to the well, whereas it remains similar to the prior for the sites that are farther.

sure, represented by a global regression line with intercept and slope. In this way, we include variabilities in the pore pressure depth trend. A third case (Case III) is considering the fact that faults are controlling the lateral fluid flow over geologic time, defining pressure compartments; i.e., fault patterns have a major control on the pressure distribution in a basin. Thus, the prior mean will depend not only on the depth but also on the pressure compartment. The replayed well situation is near the border of the two compartments in the top part of Figure 2b. In doing so, the pore pressure mean in the northern sites is obtained from one compartment, whereas southern sites have another compartment mean. The covariance matrix is obtained in the same way as for the base case.

To summarize, we have the following cases:

- Case I:
  $\mathbf{\Sigma}_{\text{new}}(\mathbf{s}_{i,k},\mathbf{s}_{j,l}) = \sigma^2_{\text{new}} \exp\left(-\frac{\sqrt{(s_{i1,k}-s_{j1,l})^2+(s_{i2,k}-s_{j2,l})^2}}{r_1} - \frac{|s_{i3,k}-s_{j3,l}|}{r_2}\right)$,
  with $\sigma^2_{\text{new}} = 2 * \sigma^2$.
- Case II: $\mathbf{\Sigma}_{\text{new}} = \mathbf{\Sigma} + \mathbf{z}\mathbf{\Sigma}_{\beta_{jl}}\mathbf{z}^T$.
- Case III: Faults control the lateral fluid flow.

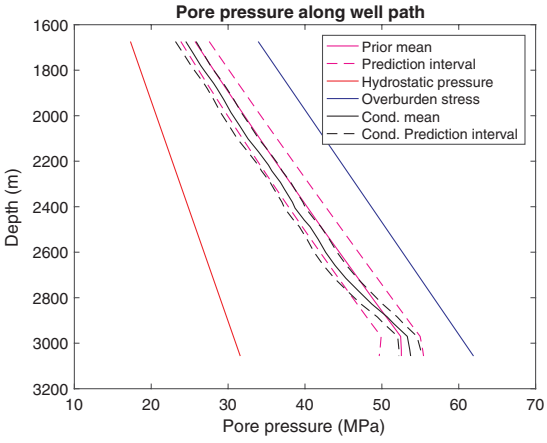

Figure 12. Prior and conditional pore pressure mean along the well path together with the respective prediction interval. There is a reduction in the uncertainty when the data assimilation procedure is complete; here, we can also spot a change in the pore pressure mean.

Table 2. Sensitivity to the prior model.

		SD values	
		143 m	0 m
Base case	Average SD	1.16	0.97
	SD at well site	1.47	0.93
Case I	Average SD	2.31	1.44
	SD at well site	2.28	1.37
Case II	Average SD	1.50	0.98
	SD at well site	1.48	0.95
Case III	Average SD	4.40	1.74
	SD at well site	4.39	1.65

The results are presented in Table 2, in which we report the SD at the planned well path site and the average SD in a horizontal plane at 143 and 0 m distance ahead of the bit.

With the larger prior uncertainty there is also a larger posterior SD, especially if we are far from the data acquisition point. When we get closer to the data acquisition point, the SD at the well site gets close to that of the base case. This can be seen as evidence of the ability of the method in reducing the uncertainty. If we look at the results of Case II in Table 2, we observe values very close to the base case. When we are 143 m from the plane, the SD is already relatively low because of the global effect term, in which updating ties up the model a bit faster.

To analyze Case III further, we plot the updated mean and SD in a horizontal plane, at the end of the well, in Figure 13. We see that the difference in pore pressure between the two compartments is very small in our case.

Because of the limited sealing capacity there is little effect here, but we suspect this could be more significant for other cases in which the lateral variation is larger.

We next study sensitivity to the likelihood model. First, we study the impact of the measurement error variance. The cases are

- Case IV: $\mathbf{R}_{\text{new}} = 4 * \mathbf{R}$.
- Case V: $\mathbf{R}_{\text{new}} = \frac{1}{4} * \mathbf{R}$.

Table 3 shows that less accurate measurements (Case IV) give a higher SD, relative to the base case. If we, vice versa, manage to get more accurate measurements, the SD is reduced, and this is particularly low in the area around the well where the data are collected.

To study which data types are more informative in our work, we analyze four different situations with subsets of data:

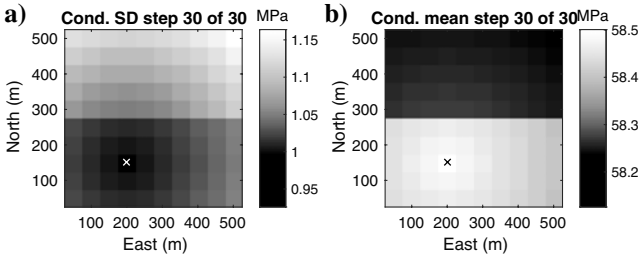

Figure 13. (a) The SD and (b) mean of pore pressure, the crosses indicate the well location. The pore pressure is showed in each site of an horizontal plane located at the same depth as the deepest point in the well. We capture the difference on pore pressure between the two compartments although the difference is small. This is due to the limited sealing capacity.

Table 3. Sensitivity to measurements error.

		SD values	
		143 m	0 m
Case IV	Average SD	1.52	1.24
	SD at well site	1.51	1.22
Case V	Average SD	1.31	0.69
	SD at well site	1.27	0.65

Table 4. Sensitivity to different data types.

		SD values	
		143 m	0 m
Case VI	Average SD	1.75	1.76
	SD at well site	1.75	1.76
Case VII	Average SD	1.70	1.45
	SD at well site	1.70	1.44
Case VIII	Average SD	1.75	1.75
	SD at well site	1.75	1.75
Case IX	Average SD	1.57	1.10
	SD at well site	1.56	1.05

- Case VI: only resistivity
- Case VII: only porosity (neutron porosity)
- Case VIII: only sonic transit time
- Case IX: porosity and sonic transit time

Table 4 shows the SD ratio values for different data types.

Studying the case with just resistivity (Case VI), the uncertainty in pore pressure is not reduced at all. In our case, the noise level is too large. Then, for cases with two data, we decide to exclude resistivity and only focus on porosity and sonic transit time. It is clear from Table 4 that having more data is better for accurate prediction of pore pressure because the SD decreases when more data are available. The transit time alone does not seem to be very informative (Case VIII), but when it is combined with porosity, the reduction of uncertainty is significant. Overall, as expected, porosity is the most informative data source for pore pressure, among the possible data studied here.

CONCLUSION

In this study, we build a prior model for pore pressure starting from predrill information of the field, and we use statistical techniques such as linear regression and variograms to incorporate trends and spatial dependencies in the model. Then, in the likelihood model, we fit links between the measurements and pore pressure. Finally, we sequentially update the pore pressure distribution with available measurements.

For the prior model, a predrill model for the pore pressure is used, resulting from pressure simulations over the geologic time scale (millions of years). The strength with this approach is that the effect of mechanical compaction and chemical compaction (illite-smectite transition in the shales) is simulated, in addition to the effect of lateral pressure transfer, mainly controlled by the fault properties and throw. Because sedimentary layers in the study are flat lying and the faults have minor throw, it results in little lateral variation in the simulated pressures. Larger lateral pressure differences are simulated and observed in other study areas such as the Halten Terrace, Norwegian Sea. We know that many of the input parameters hold large uncertainties; therefore, a Monte Carlo approach is preferred. In this study, only one simulation is used for the prior model.

The main contribution of this paper is pore pressure prediction highlighting the following points:

- Bayesian modeling: The approach provides consistent integration of predrill a priori knowledge about the pore pressure and the well-log measurements.
- Real time: The prediction of pore pressure is updated when the new well-log data are available.
- Spatial prediction: The prediction is not only done near the borehole location, but also ahead of the bit and at other lateral and depth locations.
- Uncertainty: The spatial predictions of pore pressure are represented by a mean value best prediction and a variance/covariance description.

The workflow we used for our particular case has a Gaussian prior model from predrill assessment. The linearized likelihood model for well logs allows efficient sequential Bayesian updating. Although this is a fit-for-purpose routine, the workflow is quite flexible and can be adapted in various situations. For instance, it can be applied to predrill assessment in which there are large uncertainties in depth trends, or for including other variables than pore pressure, such as more detailed information about facies classes. In addition, the measurements can include other kinds of data than what was considered here. One possibility is to evaluate the information content in formation tests, or look-ahead tools providing data for deeper locations. This can also be done in the context of improved decision making related to mud weight.

If Gaussian distributions are not realistic, another recursive updating method using stochastic simulations could be envisioned. The current workflow would then be extended to use realizations of pore pressure as the input and update these in real time when log data are available. We regard this as future work.

ACKNOWLEDGMENTS

The work is carried out as a part of the KPN project 255418/E30: "Reduced uncertainty in overpressures and drilling window prediction ahead of the bit (PressureAhead)" and is funded by the Norwegian Research Council and the DrillWell Centre (AkerBP, Wintershall, ConocoPhillips, and Statoil). ConocoPhillips contributed with input data.

DATA AND MATERIALS AVAILABILITY

Data associated with this research are confidential and cannot be released.

REFERENCES

Bektas, E., S. Z. Miska, E. M. Ozbayoglu, M. Yu, N. Takach, D. Velazquez-Cruz, and M. P. Shahri, 2015, Application of Kalman filter to predictions of pore pressure while drilling: Presented at the SPE Annual Technical Conference and Exhibition.

Bhakta, T., P. Avseth, and M. Landrø, 2016, Sensitivity analysis of effective fluid and rock bulk modulus due to changes in pore pressure, temperature and saturation: Journal of Applied Geophysics, **135**, 77–89, doi: 10.1016/j.jappgeo.2016.09.012.

Borge, H., 2000, Fault controlled pressure modelling in sedimentary basins: Ph.D. thesis, Norwegian University of Science and Technology.

Bowers, G. L., 1995, Pore pressure estimation from velocity data: Accounting for overpressure mechanisms besides undercompaction: SPE Drilling and Completion, **10**, 89–95, doi: 10.2118/27488-PA.

Chopra, S., and A. R. Huffman, 2006, Velocity determination for pore-pressure prediction: The Leading Edge, **25**, 1502–1515, doi: 10.1190/1.2405336.

Dobson, A. J., and A. Barnett, 2008, An introduction to generalized linear models: CRC Press.

Dutta, N., 2002, Geopressure prediction using seismic data: Current status and the road ahead: Geophysics, **67**, 2012–2041, doi: 10.1190/1.1527101.
Eaton, B. A., 1975, The equation for geopressure prediction from well logs: Presented at the Fall meeting of SPE of AIME, SPE.
Gholami, R., M. Rabiei, V. Rasouli, B. Aadnoy, and N. Fakhari, 2015, Application of quantitative risk assessment in wellbore stability analysis: Journal of Petroleum Science and Engineering, **135**, 185–200, doi: 10.1016/j.petrol.2015.09.013.
Goovaerts, P., 1997, Geostatistics for natural resources evaluation: Oxford University Press.
Jaeger, J., and N. Cook, 1963, Pinching-off and disking of rocks: Journal of Geophysical Research, **68**, 1759–1765, doi: 10.1029/JZ068i006p01759.
López, J. L., P. M. Rappold, G. A. Ugueto, J. B. Wieseneck, and C. K. Vu, 2004, Integrated shared earth model: 3D pore-pressure prediction and uncertainty analysis: The Leading Edge, **23**, 52–59, doi: 10.1190/1.1645455.
Lothe, A., 2004, Simulations of hydraulic fracturing and leakage in sedimentary basins: Ph.D. thesis, University of Bergen.
Lothe, A., H. Borge, and R. Gabrielsen, 2004, Modelling of hydraulic leakage by pressure and stress simulations and implications for Biot's constant: An example from the Halten terrace, offshore Mid-Norway: Petroleum Geoscience, **10**, 199–213, doi: 10.1144/1354-079303-579.
Lothe, A., P. Cerasi, K. Bjørkevoll, and S. Haavardstein, 2018, Digitized uncertainty handling of pore pressure and mud-weight window ahead of bit; example North Sea: IADC/SPE Drilling Conference and Exhibition, IADC/SPE-189665–MS.
Lothe, A., and A. Grøver, 2009, Evaluation of sealing properties to faults and cap rocks and its influence on fluid pressure distribution — Using a Monte Carlo simulation approach: Presented at theAAPG Hedberg Research Conference.
Malinverno, A., and R. L. Parker, 2006, Two ways to quantify uncertainty in geophysical inverse problems: Geophysics, **71**, no. 3, W15–W27, doi: 10.1190/1.2194516.
Malinverno, A., C. M. Sayers, M. J. Woodward, and R. C. Bartman, 2004, Integrating diverse measurements to predict pore pressure with uncertainties while drilling: Presented at theSPE Annual Technical Conference and Exhibition.
Mavko, G., T. Mukerji, and J. Dvorkin, 2009, The rock physics handbook: Tools for seismic analysis of porous media: Cambridge University Press.
Oughton, R. H., D. A. Wooff, R. W. Hobbs, R. E. Swarbrick, and S. A. O'Connor, 2017, A sequential dynamic Bayesian network for pore pressure estimation with uncertainty quantification: Geophysics, **83**, no. 2, D27–D39, doi: 10.1190/geo2016-0566.1.
Rommetveit, R., K. S. Bjorkevoll, P. R. Cerasi, S. T. Havardstein, M. Fjeldheim, H. M. Helset, S. I. Odegard, and C. Nordstrand, 2010, Real time integration of ECD, temperature, well stability and geo/pore pressure simulations during drilling a challenging HPHT well: Presented at theSPE Intelligent Energy Conference and Exhibition.
Särkkä, S., 2013, Bayesian filtering and smoothing: Cambridge University Press.
Sayers, C., L. Den Boer, Z. Nagy, P. Hooyman, and V. Ward, 2005, Pore pressure in the Gulf of Mexico: Seeing ahead of the bit: World Oil, **55**, 55–58.
Sayers, C. M., G. Johnson, and G. Denyer, 2002, Predrill pore-pressure prediction using seismic data: Geophysics, **67**, 1286–1292, doi: 10.1190/1.1500391.
Sclater, J. G., and P. A. Christie, 1980, Continental stretching: An explanation of the post-mid-cretaceous subsidence of the central North Sea basin: Journal of Geophysical Research: Solid Earth, **85**, 3711–3739, doi: 10.1029/JB085iB07p03711.
Twiss, R. J., and E. M. Moores, 1992, Structural geology: Macmillan.
Ugwu, G., 2015, An overview of pore pressure prediction using seismically derived velocities: Journal of Geology and Mining Research, **7**, 74–80, doi: 10.5897/JGMR15.0218.
Walderhaug, O., 1996, Kinetic modeling of Quartz cementation and porosity loss in deeply buried sandstone reservoirs: AAPG Bulletin, **80**, 731–745.
Wessling, S., A. Bartetzko, and P. Tesch, 2013, Quantification of uncertainty in a multistage/multiparameter modeling workflow: Pore pressure from geophysical well logs: Geophysics, **78**, no. 3, WB101–WB112, doi: 10.1190/geo2012-0402.1.
Zhang, J., 2011, Pore pressure prediction from well logs: Methods, modifications, and new approaches: Earth-Science Reviews, **108**, 50–63, doi: 10.1016/j.earscirev.2011.06.001.